

Disordered graphene and boron nitride in a microwave tight-binding analogue

S. Barkhofen,¹ M. Bellec,² U. Kuhl,^{2,1} and F. Mortessagne²

¹*Fachbereich Physik der Philipps-Universität Marburg, D-35032 Marburg, Germany*

²*Laboratoire de Physique de la Matière Condensée, CNRS UMR 7336, Université de Nice Sophia-Antipolis, 06108 Nice, France*

(Dated: November 25, 2018)

Experiments on hexagonal graphene-like structures using microwave measuring techniques are presented. The lowest coupled transverse-electric resonance of coupled dielectric discs sandwiched between two metallic plates establish a tight-binding configuration. The nearest-neighbor coupling approximation is investigated in systems with few discs. Taking advantage of the high flexibility of the discs positions, consequences of the disorder introduced in the graphene lattice on the band structures are investigated. Using two different types of discs, a boron nitride-like structure (a hexagonal lattice with a two-atom basis) is implemented, showing the appearance of a band gap.

PACS numbers: 42.70.Qs, 73.22.-f, 71.20.-b, 03.65.Nk

I. INTRODUCTION

Graphene, due to its unusual and astonishing electronic and physical properties, is a subject of intense focus, especially since it was experimentally realized in 2005 by K. S. Novoselov, A. K. Geim and coworkers [1], who were honored by the Nobel prize in physics in 2010. One of graphene's amazing features is the linear dispersion relation close to the K-points and the Dirac like Hamiltonian whose consequences can be seen in the density of states (for details on graphene see the reviews [2, 3]). Graphene is one of the candidates to take over from silicon based electronics. Graphene has a macroscopic ballistic carrier transport due to its high charge carrier mobility and a high magnetic susceptibility μ [4]. A problem is still that graphene in its pure form is metallic and has no band gap ΔE . Nevertheless a band gap can be induced by using bilayer graphene [5], disorder [6, 7], lateral-superlattice, epitaxially grown graphene on top of a crystal like boron nitride [8–10] or by confinements [11, 12]. Applying stress to graphene can induce effects on the electron transport like a magnetic field [13]. Thus graphene offers a big variety of interesting possibilities from both applied and fundamental points of view.

In real single layer graphene, it is quite difficult to prepare special shapes, induce precise structures of vacancies and so on. This can be easily performed in experiments with classical waves. For example in microwave analogue experiments, the Dirac point [14–16], the global band structures [17] and edge states [16, 17] have been observed. These states which are located only at the zig-zag edges can lead to self-guiding unidirectional electromagnetic transport if the hexagonal lattice is created by ferritic scatterers [18]. Edge states have also been found in acoustics [19].

In this paper we mimic the established tight-binding form of graphene's Hamiltonian [20–22] with a microwave setup using dielectric discs between two metallic plates. In a previous publication we investigated the Dirac point in the density of states (DoS) [16]. Here we concentrate

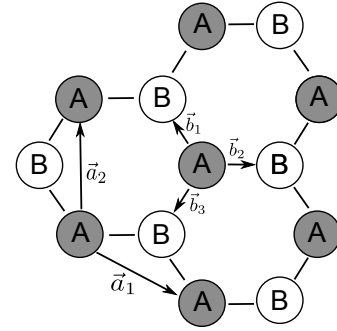


FIG. 1. (Color online) Graphene as superposition of two triangular sublattices A and B with lattice vectors \vec{a}_1 , \vec{a}_2 and the vectors \vec{b}_1 , \vec{b}_2 , \vec{b}_3 connecting nearest neighbours.

more on the experimental details of the realization of the tight-binding Hamiltonian (see Sec. III). We show the flexibility of the experimental ansatz by investigating two different cases. The first case is to introduce positional disorder, where for strong disorder the Dirac point (see Sec. IV) vanishes. The second case is to realize a boron-nitride like structure by using two different kinds of discs on the lattice (see Sec. V). In this case a band gap opens.

II. THEORETICAL BACKGROUND

Graphene is a two-dimensional crystal of carbon atoms ordered in a regular hexagonal lattice, a so-called “honeycomb” structure (see Fig. 1). It was first completely described theoretically by Wallace in 1947 [20]. The far-reaching equivalence of graphene's Hamiltonian and the Dirac Hamiltonian for a free particle is depicted in [23]. Using the order and the notation of [23] we first give a short repetition of a standard derivation of graphene's Hamiltonian to underline its equivalence to our experiment.

Graphene's characteristic honeycomb lattice structure is caused by the sp^2 -bond of the carbon atoms resulting

in three σ -bonds in the plane including an angle of 120° and a free p_z -orbital perpendicular to the plane. The bonding length between the carbon atom is $a_b = 1.42 \text{ \AA}$. The basis vectors of the hexagonal lattice – illustrated in Fig. 1 – are $\vec{a}_1 = (\sqrt{3}/2, -1/2) a$ and $\vec{a}_2 = (0, 1) a$, where $a = \sqrt{3} a_b$ is the lattice constant. The vectors connecting the two sublattices are $\vec{b}_1 = (1/2\sqrt{3}, 1/2) a$, $\vec{b}_2 = (-1/\sqrt{3}, 0) a$, and $\vec{b}_3 = (1/2\sqrt{3}, -1/2) a$. In the tight-binding approximation we assume a basis of localized eigenfunction at the lattice sites imitating the p_z -orbitals. Thus we can write down the Hamiltonian in second quantization which includes the position energy and the hopping term.

For the position term H_{pos} we use diatomic system (indicated in Fig. 1 by A and B) placed on the two triangular lattices A and B , which is realized e.g. in boron nitride. In the tight-binding model an atom of sort A only interacts with its three nearest neighbors that all belong to the lattice B (see Fig. 1). Second nearest-neighbor hopping is here neglected. The energy difference between electrons localized on lattice A and electrons on lattice B is called $\beta = (\epsilon_A - \epsilon_B)/2$. The associated part of the Hamiltonian can be written as

$$\begin{aligned} H_{\text{pos}} &= \sum_{\vec{A}} \epsilon_A n(\vec{A}) + \epsilon_B n(\vec{B}) \\ &= \beta \sum_{\vec{A}} [n(\vec{A}) - n(\vec{A} + \vec{b}_1)] + \underbrace{\frac{\epsilon_A + \epsilon_B}{2}}_{\equiv E_0} N_{\text{tot}} \quad (1) \end{aligned}$$

where $n(\vec{A})$ and $n(\vec{A} + \vec{b}_1)$ are the counting operators of electrons at positions \vec{A} belonging to lattice A and at $\vec{B} = \vec{A} + \vec{b}_1$ to lattice B , respectively. They can be written using the creation and annihilation operators U , U^\dagger , V and V^\dagger as $n(\vec{A}) = U^\dagger(\vec{A})U(\vec{A})$ and $n(\vec{A} + \vec{b}_1) = V^\dagger(\vec{A} + \vec{b}_1)V(\vec{A} + \vec{b}_1)$. $\sum_{\vec{A}}$ is the sum over all atoms of lattice A . The additional term proportional to E_0 times the total number of electrons is only a constant and can be neglected in the further treatment. It corresponds to an energy shift to the mean energy of the two atoms (for graphene to the eigenenergy of one atom).

The second part of the Hamiltonian includes the hopping of electrons from one lattice site to one of the neighboring sites. The hopping parameter κ describes the probability for this process and corresponds to the nearest-neighbor coupling, which is accessible in the measurements (see Sec. III E).

$$H_{\text{hop}} = \kappa \sum_{\vec{A}, i} [U^\dagger(\vec{A})V(\vec{A} + \vec{b}_i) + V^\dagger(\vec{A} + \vec{b}_i)U(\vec{A})] \quad (2)$$

with $i = 1, 2, 3$ for the three nearest neighbors in lattice B of an atom A. The spin of the electron is here neglected, as a spin is not existing in the microwave experiment. The entire Hamiltonian equals the sum of Eq. (1) and Eq. (2) and has the eigenenergies:

$$E(\vec{k}) = \pm \sqrt{\beta^2 + \kappa^2 \left| e^{i\vec{k} \cdot \vec{b}_1} + e^{i\vec{k} \cdot \vec{b}_2} + e^{i\vec{k} \cdot \vec{b}_3} \right|^2} \quad (3)$$

For the case of graphene ($\beta = 0$) the two bands with plus and minus signs are touching each other at the roots of the sum of the three exponential functions. These are given at $\vec{K} = \frac{2\pi}{\sqrt{3}a}(1, \sqrt{3})$ and $\vec{K}' = -\vec{K}$, the corners of the Brillouin zone. The dispersion relation is approximately linear close to these K -points with the so-called Fermi velocity v_f as the proportionality constant:

$$E(\vec{K} + \vec{q}) \approx \pm \underbrace{\frac{\sqrt{3}}{2} \kappa a}_{\equiv v_f} |\vec{q}| \quad \text{for } |\vec{q}| \ll |\vec{K}| \quad (4)$$

This equals the relativistic dispersion relation $E(\vec{p}) = \pm c|\vec{p}|$ for a massless particle, when v_f plays the role of the speed of light, and leads to the common name “Dirac points” for K and K' .

The strong connection to the Dirac theory is moreover given by the equivalence of the Dirac Hamiltonian and a certain form of graphene’s Hamiltonian which can be derived via a basis transformation described in [23].

From Eq. (4) the density of states (DoS) in the vicinity of the Dirac points can be calculated

$$\rho(E) \approx \frac{4}{\sqrt{3}\pi} \frac{|E|}{\kappa^2} \quad (5)$$

which is again linear.

In our experiments the DoS (strictly speaking the *local* density of states, LDoS) is an accessible quantity. In our previous work we have observed the linear dependence of the DoS close to the Dirac point [16]. In this paper we want to investigate the stability of the Dirac points against disorder (see Sec. IV).

If the on-site energies are different, i.e. $\beta \neq 0$ like in boron nitride then a gap is generated at the Dirac point, where the gap width is given by $2\beta = \epsilon_A - \epsilon_B$. An analogue to boron nitride is presented in Sec. V.

A. Local density of states

We derive here the relation between the measured reflection signal S_{11} at an antenna to the LDoS.

In quantum mechanics the LDoS $\mathcal{L}(\vec{r}, E)$ is defined by

$$\mathcal{L}(\vec{r}, E) \equiv \sum_n |\phi_n(\vec{r})|^2 \delta(E - E_n) \quad (6)$$

where $\phi_n(\vec{r})$ is the n^{th} eigenfunction at position \vec{r} and can be expressed via the Green function $G(\vec{r}, \vec{r}, E)$ of the system

$$\begin{aligned} \mathcal{L}(\vec{r}, E) &= -\frac{1}{\pi} \text{Im} \left(\lim_{\epsilon \rightarrow 0} \sum_n \frac{|\phi_n(\vec{r})|^2}{E - E_n + i\epsilon} \right) \\ &= -\frac{1}{\pi} \text{Im} [G(\vec{r}, \vec{r}, E)]. \end{aligned} \quad (7)$$

To relate the Green function to the reflection R^2 , let’s start with the probability T^2 for the wave to escape from

the antenna. By energy conservation it is connected to the reflection R^2 and given by

$$1 = R^2 + T^2 = |S_{11}|^2 + T^2$$

$$T^2 = 1 - |S_{11}|^2 = \oint \vec{j} \cdot d\vec{s} \quad (8)$$

where $d\vec{s}$ corresponds to a line of an area around the antenna assuming a two-dimensional setup. \vec{j} is the two-dimensional quantum mechanical probability current

$$\vec{j} = \frac{\hbar}{m} \text{Im} (\psi^* \nabla_{xy} \psi)$$

which in electrodynamics corresponds to the two-dimensional Poynting vector for TE-modes

$$\vec{S}_{xy} = -\frac{\mu^2}{\epsilon \omega} \text{Im} (B_z^* \nabla_{xy} B_z). \quad (9)$$

We neglect the prefactors because only the proportionality of the current to $\text{Im}(\psi^* \nabla_{xy} \psi)$ is important. In approximation of a point-like excitation in \vec{R} the wave function $\psi = B_z$ is proportional to the Green function $G(\vec{r}, \vec{R}, E)$, as both are the solution of the Helmholtz differential equation with delta inhomogeneity. The proportionality coefficient $\Lambda(E, \vec{R})$ depends on the coupling of the antenna to the system. Combining Eq. (7), Eq. (8) and Eq. (9) we obtain:

$$1 - |S_{11}|^2 \propto -|\Lambda(E, \vec{R})|^2 \oint \text{Im} \left[G^*(\vec{r}, \vec{R}, E) \nabla_{xy} G(\vec{r}, \vec{R}, E) \right] d\vec{s}$$

$$\propto |\Lambda(E, \vec{R})|^2 \text{Im} \xi_\beta(\vec{R}, E)$$

$$\propto |\Lambda(E, \vec{R})|^2 \mathcal{L}(\vec{R}, E)$$

where the renormalised Green function

$$\xi_\beta(\vec{R}, E) = \lim_{\vec{r} \rightarrow \vec{R}} \left[G(\vec{r}, \vec{R}, E) - \frac{1}{2\pi} \ln \left(\frac{|\vec{r} - \vec{R}|}{\beta} \right) \right] \quad (10)$$

guarantees the avoidance of singularities at the antenna positions \vec{R} . β is the scattering length of the antenna. A detailed derivation of the renormalized Green function can be found in [24].

It is not clear how the coupling parameter $\Lambda(E, \vec{R})$ depends on E or even on the LDoS. Therefore it is necessary to find a proper coupling theory. With the methods developed in [24] it is possible to derive an approximative description of the coupling for small cylindrical antennas showing an almost frequency independent prefactor $\Lambda(E, \vec{R})$. Hence we finally obtain the relation between the LDoS and the reflection which is given by

$$\mathcal{L}(R, E) \propto 1 - |S_{11}(R, E)|^2 \quad (11)$$

Based on this knowledge we will plot in the following figures $1 - |S_{11}|^2$ on the y -axis.

III. EXPERIMENTAL REALISATION OF A TIGHT-BINDING SYSTEM

A. Introducing microwave experiments

Microwave experiments have been proven to be an attractive implementation to perform quantum analogue measurements in the realm of “quantum chaos” since 20 years [25, 26]. Exploiting the formal analogy of the Helmholtz and the Schrödinger equation they have been used to investigate many different effects like eigenvalue distributions, nodal domains [27, 28], affirmation of periodic orbit theory [29, 30], random matrix theory [31, 32] and the random plane wave model [33]. Quantum mechanical currents and the visualisation of chaotic wave functions in billiard systems [34, 35] have already been in the center of attention. Nowadays the area of application became much wider and reaches beyond the first investigations on chaotic billiards. For instance one-dimensional wave guides with introduced disorder have been suitable to check scattering theory phenomena [36]. Effects of uncorrelated and correlated disorder have been observed [37–39] and localisation phenomena have been investigated in two dimensional systems using dielectric discs [40].

Transport of electrons in lattices is related to wave phenomena. As large interest in the special properties of the band structure of graphene occurred, microwave analogue experiments have been performed on graphene like structures using different kind of realizations [14–17]. Here we want to emphasize the possibilities of using dielectric discs with an high index of refraction [16]. This new field offers a high flexibility to realize random or symmetric lattice structures and investigate its characteristics by observing the local density of states at different positions.

B. The setup

For the investigation of tight-binding systems we need wave functions which live in a finite volume and decrease faster as $\frac{1}{|\vec{r}|^2}$ outside. This scenario can be considered as a potential well configuration. For the realization we chose dielectric discs (Temex-ceramics, E2000 series) with a dielectric permittivity $\epsilon_r \approx 36$ and a relative permeability $\mu_r = 1$. They have a diameter of 8 mm and a height of 5 mm (see inset of Fig. 2).

These discs were previously used to realize disordered systems [40]. They are placed between two metallic plates separated by a distance h . The height h is smaller than a maximal height h_{cut} guaranteeing that the TE-waves are evanescent outside the disc, i.e. the cut-off frequency given by $\nu_{cut}(\vec{r}) = \frac{c_0}{2h}$ is larger than the investigated resonance frequency of the discs. This assures additionally the two-dimensionality of the system [26]. Further descriptions about the disc eigenmodes are given in Sec. III C.

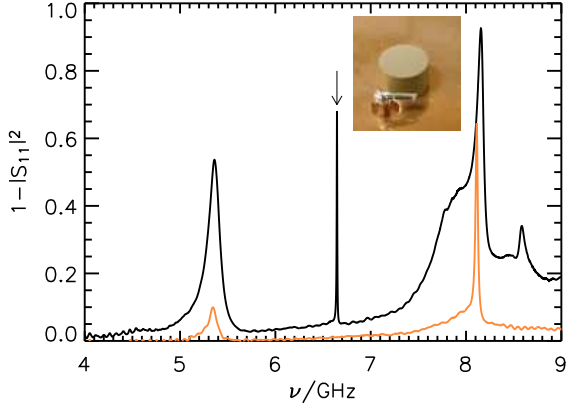


FIG. 2. (Color online) Spectrum of a single disc: Black line corresponds to a measurement with the TE-antenna shown in the inset; orange line shows the same measurement performed with a TM-antenna. The arrow marks the first TE-resonance which will be used for the further experiments (from [16]).

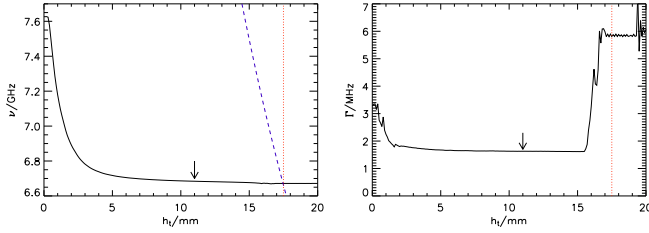


FIG. 3. (Color online) Resonance frequency ν (left) and width Γ (right) of a single disc are shown in dependence of the distance h_t between the metallic top plates and the top of the disc. The dashed blue line corresponds to the cut-off frequency at the corresponding height and the vertical dotted red line indicates the height at which the resonance frequency is above the cut-off frequency. The arrow marks the chosen distance $h_t = 11$ mm between the top of the disc to the top plate for the experiments.

In Fig. 2 the reflection spectra are shown using two different kind of antennas. The first is a pure dipole antenna, which consists of a vertical part, exciting only TM modes (shown in orange). The second has an additional kink (see inset) and can also excite the TE modes (spectrum shown in black). The sharp resonance marked by the arrow is the TE₁ resonance of the disc as it is not observable with a dipole antenna. Besides it is nicely separated from the neighboring resonances and has a quite flat background. Thus it is a suitable resonance for further investigations. We always make sure that the other resonances are still separated from the frequency range of this TE-resonance so that mixing or overlapping of TE and TM modes are avoided. Consequently we work in a one-level regime, where each disc brings in only a single resonance.

To mimic molecules or solids several discs have to be placed between the top and bottom plate ensuring each of them has the same eigenfrequency. One problem for

this realization is the sensitivity of the resonance frequency once the top plate is very close to the top of the discs. This can be seen in Fig. 3, where the resonance frequency and width is shown in dependence of the distance h_t between the disc top and the metallic top plate. At $h_t=0$ mm the bottom plate is pressed against the upper plate using a step motor. Thereafter it is moved in steps of 0.1 mm. At the beginning this just corresponds to a release of the pressure and thus the resonance frequency does not change. Otherwise for small distances the change of resonance frequency is larger than the resonance width. For larger distances the resonance frequency stabilises. The width decays for small distances and stabilises also but increases strongly once the eigenfrequency gets closer to the cut-off frequency. For all further measurements a height of $h=16$ mm ($h_t=11$ mm) is chosen to guarantee sharp and stable resonances.

The discs are positioned by a motorized xy -stage that is controlled by a PC programme. Hence it is possible to create structures of a few hundreds of discs with an accuracy of the order of 0.1 mm. To ensure good and equivalent contact of the discs to the bottom plate the discs are pushed down while placing them.

C. Disc eigenmodes

The aim of our experiment is to realize a tight-binding system of localized functions with weak coupling to the outside. For the theoretical description, let's assume that $h_t=0$ mm, i. e. the top plate touches the disc, the refractive index is $n = 6$, and the disc height is $h = 5$ mm. The TE₁ mode consists only of the z -component of the magnetic field $\vec{B} = (0, 0, B_z)$ and the perpendicular components of the electric field. The distance between top and bottom plates defines the cut-off frequencies $\nu_{\text{air}} = \frac{c_0}{2nh} = 9.37$ GHz in air ($n = 1$) and $\nu_{\text{disc}} = 4.98$ GHz inside the discs for this first TE-mode. The z -dependence can be separated and if the resonance frequency is between the two cut-off frequencies the lowest TE resonance then looks like:

$$B_z(x, y, z, k) = B_0 \times \begin{cases} \sin\left(\frac{\pi}{nh}z\right) J_0(k_{\perp}r); & r < r_D \\ \alpha \sin\left(\frac{\pi}{h}z\right) K_0(\gamma r); & r > r_D \end{cases} \quad (12)$$

where $k_{\perp} = \sqrt{k^2 - \left(\frac{\pi}{nh}\right)^2}$, $\gamma = \sqrt{\left(\frac{\pi}{h}\right)^2 - k^2}$, and $r = \sqrt{x^2 + y^2}$ is the distance from the center of the disc. J_0 and K_0 are Bessel functions and α is a constant to be determined from the continuity equations at the surface. At the resonance frequency of the disc, the wave number for $r > r_D$ is thus purely imaginary leading to an evanescent wave in the area outside the disc. Note that in the experiment there is a gap between the top plate and the discs, and this description is only valid approximately. We still use Eq. (12) but with an effective γ to be determined from the experiment.

To experimentally test the wave function inside the disc, we measured the reflection as a function of the posi-

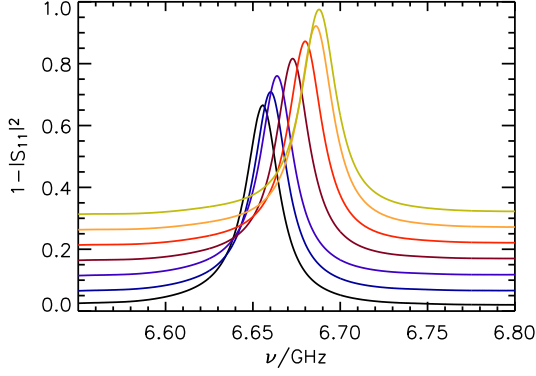


FIG. 4. (Color online) Lowest (black) spectrum: no perturber, next (blue) spectrum: Perturber close to the border, the further up shifted the spectrum, the closer is the perturber placed to the disc's center. The spectra are shifted in y in steps of 0.05 for better visualisation.

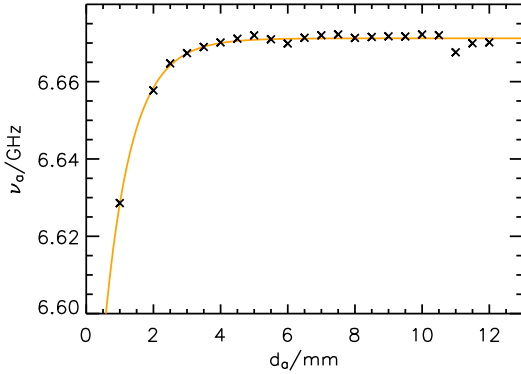


FIG. 5. (Color online) Resonance positions ν_{exp} versus distance between disc and antenna (black crosses) with fit of Eq. (13) (orange) with $\kappa_a = -13.8917$ GHz, $\gamma = 0.5198 \text{ mm}^{-1}$, and $\nu_0 = 6.6712$ GHz.

tion of a perturber, i.e. a small metallic rod placed above the disc. For this measurement the top plate is removed. The perturber induces a frequency shift which is proportional to the intensity of the wave at the position of the perturber. In Fig. 4 a monotonous resonance shift is observed confirming that the wave function corresponds to the lowest Bessel function J_0 . A direct coupling of the TE_1 mode to the TM_0 and TM_1 mode is strongly suppressed by the continuity conditions of the fields at the disc boundaries. Consequently the wave function in the discs can be identified with an electron wave localized at a lattice site.

D. Impact of the measuring antenna

For all the measurements we need to know the impact of the antenna on the disc eigenmode. Hence the coupling between two different objects, i.e. disc and antenna, is investigated. The pure presence of the antenna disturbs the symmetry of the system, but the coupling behavior can be quantified in a simple measurement series: we use a single disc with radius r_D and increase its distance d_a to the antenna and focus on the shift of the resonance. The corresponding resonances can be seen in Fig. 5. For smaller couplings, i.e. for larger distances, the resonance frequency becomes higher and its amplitude decreases. As the resonance shifts for vanishing coupling to the pure eigenresonance, we can assume the eigenfrequency of the unperturbed disc to be 6.67 GHz. The shift of the resonance due to the antenna is proportional to the wave function's intensity at the position of the antenna, i.e. at distance $r_D + d_a$. Thus we fit the following function

$$\nu_a(d_a) = \kappa_a |K_0[\gamma(r_D + d_a)]|^2 + \nu_0 \quad (13)$$

to the data points, where we have an additive constant for the unperturbed eigenfrequency ν_0 and the three fitting parameters κ_a , γ , ν_0 to the experimentally observed resonance frequency ν_a .

In Fig. 5 the experimental values are shown. A good agreement between fit (see orange line) and data points (crosses) is found and we obtained the parameters as $\kappa_a = -13.8917$ GHz, $\gamma = 0.5198 \text{ mm}^{-1}$, and $\nu_0 = 6.6712$ GHz. It's worth noting that κ_a also includes the global coupling characteristics of the antenna. For an infinite distance the pure eigenfrequency $\nu_0 = 6.6712$ GHz remains and defines the eigenenergy of an isolated disc. Let's now examine the disc-disc coupling.

E. Extracting the coupling parameter in two disc measurements

A system consisting of two discs with slightly different eigenfrequencies ν_0 and $\nu_0 + \Delta\nu_0$ and a distance depending coupling $\kappa_1(d)$ can be described by the Hamiltonian

$$H(d) = \begin{pmatrix} \nu_0 & \kappa_1(d) \\ \kappa_1(d) & \nu_0 + \Delta\nu_0 \end{pmatrix} \quad (14)$$

where the chosen basis (1, 0) and (0, 1) means “electron” in eigenstate of disc 1 with eigenfrequency ν_0 and eigenstate of disc 2 with eigenfrequency $\nu_0 + \Delta\nu_0$, respectively. The difference $\Delta\nu_0$ of the eigenfrequencies includes the influence of the antenna, quantified in Sec. III D, and the discrepancy between the discs.

The Hamiltonian has the eigenvalues

$$\nu_{1,2}(d) = \nu_0(d) + \frac{1}{2}\Delta\nu_0 \pm \frac{1}{2}\sqrt{4\kappa_1(d)^2 + \Delta\nu_0^2}$$

whose difference is given by

$$\Delta\nu(d) = \sqrt{4\kappa_1(d)^2 + \Delta\nu_0^2}$$

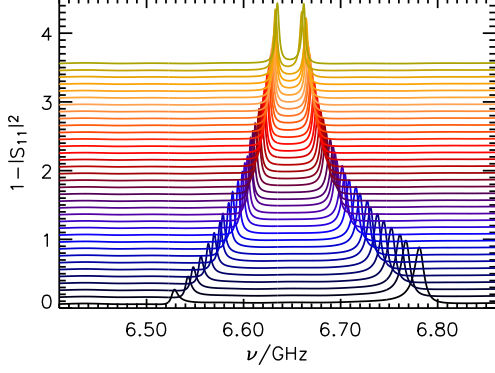


FIG. 6. (Color online) Two disc spectra for increasing distance. They are up-shifted with increasing distance. The lowest spectrum corresponds to a distance of 0.6 mm, the top-most to 7.6 mm.

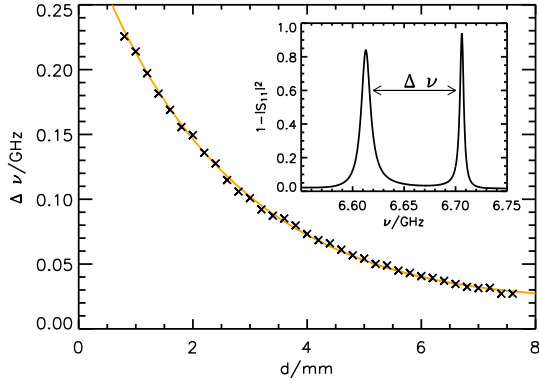


FIG. 7. (Color online) Resonance splitting of the two disc system depending on the disc distance (black crosses). The experimental data agrees well with the fit function Eq. (16) for values $\kappa_0 = 1.35$ GHz, $\gamma = 0.288 \text{ mm}^{-1}$ and $\Delta\nu_0 = 0.021$ GHz. The inset shows exemplary the spectrum for $d = 3.3$ mm (from [16]).

The coupling can be calculated by the overlap of the wave function of the single discs. Using the evanescent waves (Eq. (12) for $r > r_D$) outside the discs the coupling is approximately given by

$$\kappa_1(d) = \kappa_0 \left| K_0 \left[\gamma \left(r_D + \frac{1}{2} d \right) \right] \right|^2. \quad (15)$$

For the shift of the resonance we thus obtain

$$\Delta\nu(d) = \sqrt{4 \kappa_0^2 \left| K_0 \left[\gamma \left(r_D + \frac{1}{2} d \right) \right] \right|^4 + \Delta\nu_0^2} \quad (16)$$

To check it experimentally we varied the coupling between two discs by increasing their distance in steps of 0.2 mm and measured the splitting of the two resonances. Figure 6 shows the corresponding spectra for distances of 0.6 mm to 7.6 mm between the borders of the discs.

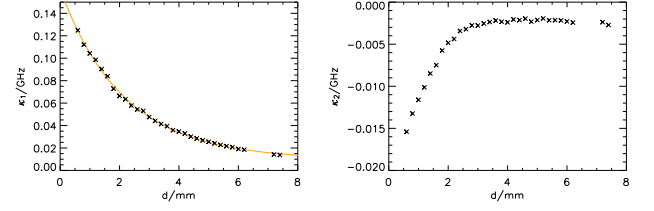


FIG. 8. Coupling parameters for three disc measurement. Left figure shows the nearest-neighbour coupling κ_1 with a fit of Eq. (15) and the right figure the extracted values for the next nearest-neighbour coupling κ_2 .

With increasing distance the decrease of the resonance splitting due to weaker coupling is clearly observable. After fitting the resonances with Lorentzians we can extract the resonance splitting depending on the distances of the discs (see Fig. 7 crosses). The experimental findings are described by Eq. (16) and by fitting we obtained $\kappa_0 = 1.35$ GHz, $\gamma = 0.288 \text{ mm}^{-1}$, and $\Delta\nu_0 = 0.021$ GHz. In the next section we probe the tight-binding approximation by quantifying the second nearest-neighbour coupling in a three disc measurement.

F. Extracting the next nearest-neighbor coupling parameter

We performed an analogous measurement with three discs in a row whose distances will be equally increased in 0.2 mm steps. The antenna remains close to the central disc. For simplicity, we neglect in the modeling of such a situation the influence of the antenna and assume perfectly equal discs. This leads to a Hamiltonian like

$$H(d) = \begin{pmatrix} \nu_0 & \kappa_1(d) & \kappa_2(d) \\ \kappa_1(d) & \nu_0 & \kappa_1(d) \\ \kappa_2(d) & \kappa_1(d) & \nu_0 \end{pmatrix}$$

with κ_1 the nearest-neighbor coupling and κ_2 the second nearest-neighbor coupling. From its three eigenvalues $\nu_{1,2,3}$ the expressions for the coupling can be calculated:

$$\kappa_1(d) = \frac{\sqrt{2\nu_1^2 + \nu_1\nu_2 - \nu_2^2 - 5\nu_1\nu_3 + \nu_2\nu_3 + 2\nu_3^2}}{3\sqrt{2}}$$

$$\kappa_2(d) = \frac{1}{3} (\nu_1 - 2\nu_2 + \nu_3)$$

The experimental findings are presented in Fig. 8. Fitting the next nearest-neighbour coupling with the same function as in Sec. III E we got

$$\frac{\kappa_1(d)}{\text{GHz}} = 2.9254 \left| K_0 \left[0.3623 \left(4 + \frac{1}{2} \frac{d}{\text{mm}} \right) \right] \right|^2 + 0.0090$$

which is similar to the fit values obtained for κ_1 in the two disc experiment underlining the consistency of the coupling theory. To justify the tight-binding approximation we investigate the ratio $|\kappa_2/\kappa_1|$, which is

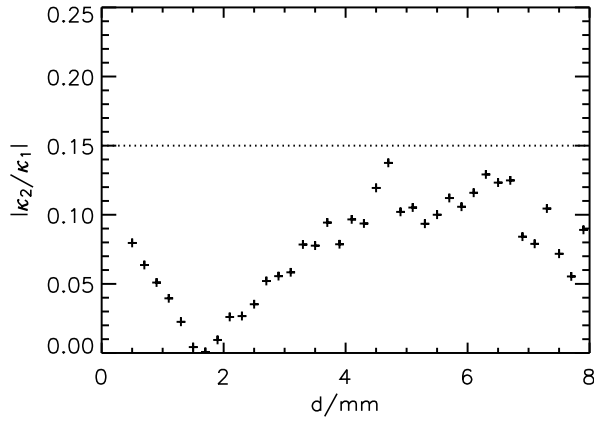


FIG. 9. (Color online) Ratio of coupling parameters for increasing distance of the disc. The second nearest neighbour coupling reaches only less than 15% of the nearest neighbour coupling (horizontal line).

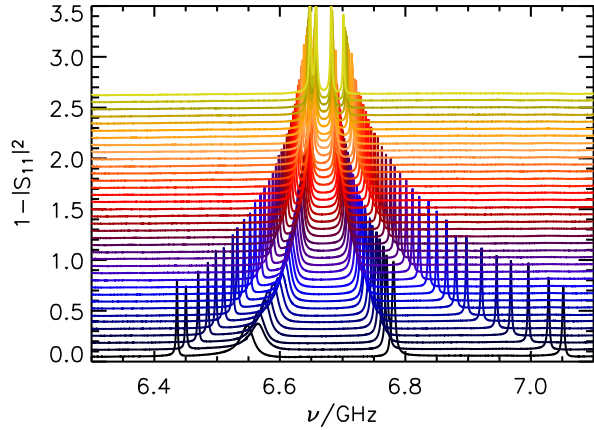


FIG. 10. (Color online) Spectra of hexagonal cells (benzene) for different distances. The spectra are up-shifted with increasing distance. The lowest spectrum corresponds to a distance of 4.5 mm, increasing in steps of 0.2 mm.

presented in Fig. 9. The ratio is always smaller than 15% thus the effects of next nearest-neighbor couplings are small but not negligible. While generally ignored in graphene next nearest-neighbor and even next-next nearest-neighbor couplings are of the order of 5% and can be even larger in bilayer or doped graphene [21, 41, 42]. Depending on the investigated properties the effects are not insignificant [21, 41, 42].

G. Benzene- the main component of graphene

The next measurements were performed on a hexagonal cell. In the following it will be called “benzene” though only the 6 p_z orbitals of the carbon atoms are imitated and their hydrogen atoms are ignored. For symmetry considerations it does not make any difference.

First we check the predictions of group theory: as ben-

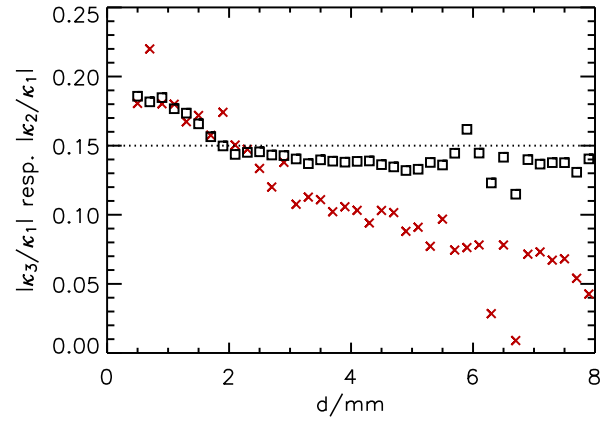


FIG. 11. (Color online) Ratios κ_3/κ_1 (crosses) and κ_2/κ_1 (squares) versus the distance. From a distance of 2 mm the ratios are smaller than 0.15 (horizontal line).

zene has the dihedral symmetry D_{6h} we expect four resonances, consisting of two singlets and two doublets. The highest and lowest resonance are not degenerate. We measured spectra of benzene for different cell radius increasing in steps of 0.2 mm. The different spectra are shown in Fig. 10 and for each we find the expected 4 resonances. The degeneracy of the two central resonances was shown in [16]. From the spectra we extract the four coupling constants from the obtained resonance differences. We obtain a fit function of the following form for κ_1

$$\frac{\kappa_1(d)}{\text{GHz}} = 2.2784 \left| K_0 \left[0.3299 \left(4 + \frac{1}{2} \frac{d}{\text{mm}} \right) \right] \right|^2 + 0.0068$$

which is consistent with the two discs and three discs measurements. Again we have a look at the ratios of the three coupling parameters which are illustrated in Fig. 11. We see that for distances larger than 2 mm both ratios are smaller than 15% which defines the tight-binding regime (horizontal dashed line). Consequently we work with disc distances from 2 mm for the following measurements on graphene flakes.

Summarizing the basic measurements on few discs we conclude the following. The group theoretical predictions are fulfilled verifying the symmetry considerations. A consistent coupling behavior is found with small second and third nearest neighbor coupling. Thus we have realized a possibility to investigate tight-binding systems with a table top experiment, where several parameters can be varied easily. Now we proceed with hexagonal lattices.

Experimental results on graphene using the same setup have already been published in [16], where the Dirac point including the linear dispersion relation close to it have been observed. Additionally edge states at zigzag edges and the lack of edge states at armchair edges have been shown. Here we will proceed by showing the flexibility of the experiment and investigate the effect of positional (coupling) disorder on the Dirac point. Addition-

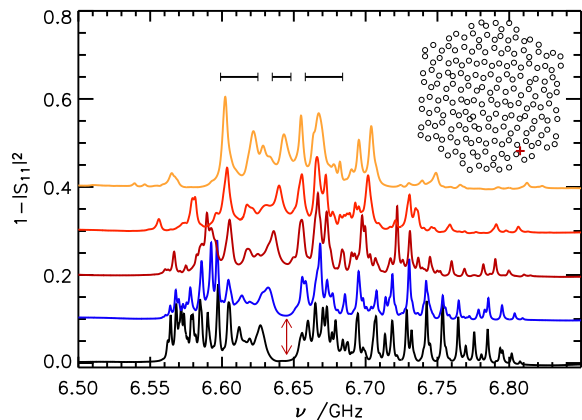


FIG. 12. (Color online) The inset on the upper right shows the graphene flake of hexagonal shape with maximal deposition of $\sigma=4$ mm. The antenna position is marked by the red cross. The spectra of the hexagonal graphene flakes with different maximal random deposition σ are shown. The lowest (black) spectrum corresponds to the unperturbed one ($\sigma=0$ mm). The spectra with $\sigma=1, 2, 3$ and 4 mm are shifted upwards correspondingly. The bars indicate the region of averaging used in Fig. 13.

ally it is possible to use different kind of discs, where we will realize a correspondence to boron nitride by using two type of discs on the two triangular sublattices.

IV. DISORDERED GRAPHENE

Graphene's astonishing DoS is a consequence of its highly symmetric hexagonal lattice structure. But in the real world the perfect hexagonal symmetry of graphene will be distorted by different means. For examples external strain [13], vacancies [6], matching to substrates [43], edges, and corners will destroy the symmetry. Additionally they can introduce disorder, e.g. via the position of vacancies in the bulk [6] or via the edges in finite systems [7]. Effects of Anderson localization have been numerically observed in transport through graphene nanoribbons with rough surfaces [44].

One kind of perturbation which can be easily modeled by our setup is bulk disorder within the disc position, i. e., disorder in the coupling. We want to test how stable the Dirac point is against an introduced disorder. To reduce effects of edge and corner states we chose a hexagonal graphene flake as shown in the inset of Fig. 12. The antenna position where the reflection S_{11} is measured is marked by a red cross. Starting with a regular lattice with a disc to disc distance of 4 mm we add to every disc position a noise, equally distributed in angle and radius and with a maximum distance to the original position of $\sigma = 1, 2, 3$, and 4 mm, respectively. The behavior of the LDoS is shown in Fig. 12. For the smallest shift we find a quite similar spectrum and can still see a strong

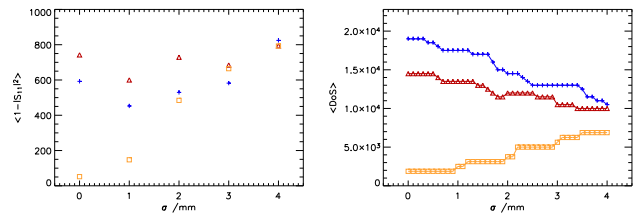


FIG. 13. (Color online) On the left the frequency averaged local density of states $\langle 1 - |S_{11}|^2 \rangle$ around the Dirac point (squares) and within the bands at lower (crosses) and higher (triangles) frequencies than the Dirac point are shown for different maximal disorder σ . The windows for averaging are indicated in Fig. 12. On the right the numerically obtained averaged DoS is presented. Symbols are used correspondingly to figure on the left.

reminiscence of the Dirac point in the LDoS (red arrow). For bigger shifts the structure disappears and the Dirac point becomes unobservable.

To investigate this in a more quantitative manner we perform averages over small frequency windows. The averaging windows are indicated by bars in Fig. 12 and are 13 MHz close to the Dirac point and 26 MHz inside the bands. By averaging fluctuations due to small frequency shifts of resonances are suppressed. In Fig. 13 on the left the averaged LDoS ($\langle 1 - |S_{11}|^2 \rangle$) is presented around the Dirac point (squares) and within the two bands (triangles and crosses). One observes with increasing disorder an increase at the Dirac point, whereas the averaged LDoS within the bands oscillates. At a maximal displacement of $\sigma=2$ mm the averaged values are of the same order, thus indicating the final vanishing of the Dirac point.

Additionally we performed numerical simulations on the same flake as in the experiment including more than only nearest neighbor couplings. We diagonalised the Hamiltonian

$$H_{tb} = \nu_0 \mathbb{1} + \mathbb{K} \quad (17)$$

where $\nu_0 = 6.65$ GHz is the eigenfrequency of one disc. The coupling matrix \mathbb{K} contains the coupling elements κ which are calculated via the disc distances using Eq. (15). The DoS is obtained by diagonalizing the Hamiltonian. On the right in Fig. 13 the averaged DoS is shown. The average is performed over the same frequency windows as in the experimental case, but here the DoS is shown and not the LDoS. One observes also here that the density close to the Dirac point is increasing. Each step actually corresponds to one additional state inside the averaging region. Within the bands a decrease of the averaged density of states is found. Overall the Dirac point seems to be quite stable against the introduction of small white noise disorder.

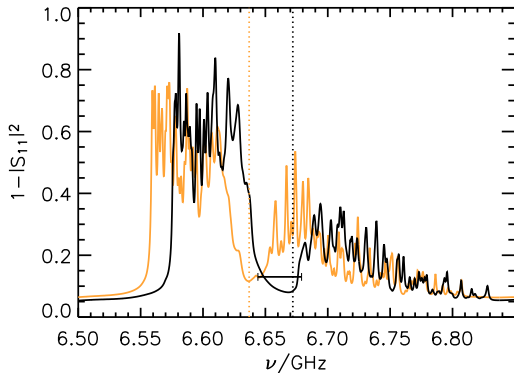


FIG. 14. (Color online) Two spectra of the same lattice configuration, but consisting of one type of discs (orange) respectively two types of discs (black). The disc close to the measuring antenna was not moved, to guarantee a consistent coupling. The dotted lines correspond to the eigenfrequencies of the two type of discs. The black bar underlines the widening of the Dirac gap.

V. IMITATING BORON NITRIDE

Boron nitride has a hexagonal lattice structure, but with two different sorts of atoms placed on the two triangular sublattices. On the applied point of view double layer of boron-nitride graphene lattices are a candidate to have on the one hand a band gap of similar energy than silicon and on the other hand keep the high charge carrier mobility of graphene [45].

The energy difference β of the two type of atoms causes a widening of the band gap between the conducting and the valence band, corresponding to Eq. (3). We imitate this situation using two charges of discs with mean eigenfrequency of 6.637 GHz respectively 6.672 GHz and create the same lattice once with equal discs and once with the different discs. A comparison of the resulting LDoS is presented in Fig. 14. The orange curve corresponds to a graphene lattice with the Dirac point at 6.637 GHz (indicated by the vertical dotted orange line). The black

curve shows the LDoS in case of the boron nitride. A gap and a corresponding shift of the gap is observed. The shift is due to the fact that we use here two different discs. Thus the center of the band is expected to be at $\frac{1}{2} (6.637 + 6.672)$ GHz = 6.655 GHz, which is in good agreement with the experiment. The gap width is expected to be $\Delta\nu_g = |(6.637 - 6.672)|$ GHz = 0.035 GHz, which is indicated by the bar and is in good agreement with the experiment as well.

VI. CONCLUSIONS

In this paper we present experimental results of hexagonal tight-binding configurations in a microwave setup. First, we show in detail why a tight-binding setup is realized. For setups with few discs we compare next-nearest neighbor coupling to the nearest neighbor coupling. The flexibility of the experiment allows to vary easily discs positions, i.e. the coupling, but also the 'on-site energies', i.e. eigenfrequency of the discs. We choose exemplarily to investigate disordered graphene. The disorder measurements show that the Dirac points seems to be quite stable against white noise disorder. As a second example showing the variation of the on-site energy we observe a band gap by using two different type of discs corresponding to a boron nitride sheet.

Exploiting the flexibility of the setup the realization of many different tight-binding structures are imaginable. Realizing different kind of vacancies including disorder, transport properties along lattice axes, or playing with K and K' points by lattice deformations [46, 47] are envisaged.

ACKNOWLEDGMENTS

This work was supported by the Deutsche Forschungsgemeinschaft via an individual grant and the Forschergruppe 760: Scattering systems with complex dynamics. S. B. thanks the LPMC at Nice for the hospitality during several long term visits and the University of Nice and the Fédération Döblin for financial supports.

-
- [1] K. S. Novoselov, A. K. Geim, S. V. Morozov, D. Jiang, M. I. Katsnelson, I. V. Grigorieva, S. V. Dubonos, and A. A. Firsov, *Nature*, **438**, 197 (2005).
 - [2] A. H. Castro Neto, F. Guinea, N. M. R. Peres, K. S. Novoselov, and A. K. Geim, *Rev. Mod. Phys.*, **81**, 109 (2009).
 - [3] A. K. Geim and K. S. Novoselov, *Nature Materials*, **6**, 183 (2007).
 - [4] F. Schedin, A. K. Geim, S. V. Morozov, E. W. Hill, P. Blake, M. I. Katsnelson, and K. S. Novoselov, *Nature Materials*, **6**, 652 (2007).
 - [5] Y. Zhang, T.-T. Tang, C. Girit, Z. Hao, M. C. Martin, A. Zettl, M. F. Crommie, Y. R. Shen, and F. Wang, *Nature*, **459**, 820 (2009).
 - [6] N. M. R. Peres, F. Guinea, and A. H. C. Neto, *Phys. Rev. B*, **73**, 125411 (2006).
 - [7] E. R. Mucciolo, A. H. Castro Neto, and C. H. Lewenkopf, *Phys. Rev. B*, **79**, 075407 (2009).
 - [8] I. Forbeaux, J.-M. Themlin, and J.-M. Debever, *Phys. Rev. B*, **58**, 16396 (1998).
 - [9] C. Berger, Z. Song, T. Li, X. Li, A. Y. Ogbazghi, R. Feng, Z. Dai, A. N. Marchenkov, E. H. Conrad, P. N. First, and W. A. de Heer, *J. Phys. Chem. B*, **108**, 19912 (2004).
 - [10] C. R. Dean, A. F. Young, I. Meric, C. Lee, L. Wang,

- S. Sorgenfrei, K. Watanabe, T. Taniguchi, P. Kim, K. L. Shepard, and J. Hone, *Nat. Nano.*, **5**, 722 (2010).
- [11] V. Atanasov and A. Saxena, *Phys. Rev. B*, **81**, 205409 (2010).
- [12] L. Huang, Y.-C. Lai, and C. Grebogi, *Phys. Rev. E*, **81**, 055203(R) (2010).
- [13] N. Levy, S. A. Burke, K. L. Meaker, M. Panlasigui, A. Zettl, F. Guinea, A. H. C. Neto, and M. F. Crommie, *Science*, **329**, 544 (2010).
- [14] S. R. Zandbergen and M. J. A. de Dood, *Phys. Rev. Lett.*, **104**, 043903 (2010).
- [15] S. Bittner, B. Dietz, M. Miski-Oglu, P. O. Iriarte, A. Richter, and F. Schäfer, *Phys. Rev. B*, **82**, 014301 (2010).
- [16] U. Kuhl, S. Barkhofen, T. Tudorovskiy, H.-J. Stöckmann, T. Hossain, L. de Forges de Parny, and F. Mortessagne, *Phys. Rev. B*, **82**, 094308 (2010).
- [17] S. Bittner, B. Dietz, M. Miski-Oglu, and A. Richter, *Phys. Rev. B*, **85**, 064301 (2012).
- [18] Y. Poo, R. x. Wu, Z. Lin, Y. Yang, and C. T. Chan, *Phys. Rev. Lett.*, **106**, 093903 (2011).
- [19] W. Zhong and X. Zhang, *Phys. Lett. A*, **375**, 3533 (2011).
- [20] P. R. Wallace, *Phys. Rev.*, **71**, 622 (1947).
- [21] S. Reich, J. Maultzsch, C. Thomsen, and P. Ordejó, *Phys. Rev. B*, **66**, 35412 (2002).
- [22] A. Matulis and F. M. Peeters, *Am. J. Phys.*, **77**, 595 (2009).
- [23] G. W. Semenoff, *Phys. Rev. Lett.*, **53**, 2449 (1984).
- [24] T. Tudorovskiy, R. Höhmann, U. Kuhl, and H.-J. Stöckmann, *J. Phys. A*, **41**, 275101 (2008).
- [25] H.-J. Stöckmann and J. Stein, *Phys. Rev. Lett.*, **64**, 2215 (1990).
- [26] H.-J. Stöckmann, *Quantum Chaos - An Introduction* (University Press, Cambridge, 1999).
- [27] U. Kuhl, R. Höhmann, H.-J. Stöckmann, and S. Gnutzmann, *Phys. Rev. E*, **75**, 036204 (2007).
- [28] B. Dietz, T. Friedrich, M. Miski-Oglu, A. Richter, and F. Schäfer, *Phys. Rev. E*, **78**, 045201(R) (2008).
- [29] M. Kollmann, J. Stein, U. Stoffregen, H.-J. Stöckmann, and B. Eckhardt, *Phys. Rev. E*, **49**, 1(R) (1994).
- [30] D. Laurent, O. Legrand, and F. Mortessagne, *Phys. Rev. E*, **74**, 046219 (2006).
- [31] U. Kuhl, R. Höhmann, J. Main, and H.-J. Stöckmann, *Phys. Rev. Lett.*, **100**, 254101 (2008).
- [32] B. Dietz, T. Friedrich, H. L. Harney, M. Miski-Oglu, A. Richter, F. Schäfer, and H. A. Weidenmüller, *Phys. Rev. E*, **78**, 055204(R) (2008).
- [33] U. Kuhl, *Eur. Phys. J. Special Topics*, **145**, 103 (2007).
- [34] S. Sridhar, *Phys. Rev. Lett.*, **67**, 785 (1991).
- [35] J. Stein and H.-J. Stöckmann, *Phys. Rev. Lett.*, **68**, 2867 (1992).
- [36] U. Kuhl, *Mikrowellenuntersuchungen an eindimensionalen Streusystemen und in zweidimensionalen Kavitäten*, Ph.D. thesis, Philipps-Universität Marburg (1998).
- [37] U. Kuhl, F. M. Izrailev, A. A. Krokhin, and H.-J. Stöckmann, *Appl. Phys. Lett.*, **77**, 633 (2000).
- [38] U. Kuhl, F. M. Izrailev, and A. A. Krokhin, *Phys. Rev. Lett.*, **100**, 126402 (2008).
- [39] O. Dietz, U. Kuhl, H.-J. Stöckmann, N. M. Makarov, and F. M. Izrailev, *Phys. Rev. B*, **83**, 134203 (2011).
- [40] D. Laurent, O. Legrand, P. Sebbah, C. Vanneste, and F. Mortessagne, *Phys. Rev. Lett.*, **99**, 253902 (2007).
- [41] J. L. McChesney, A. Bostwick, T. Ohta, T. Seyller, K. Horn, J. González, and E. Rotenberg, *Phys. Rev. Lett.*, **104**, 136803 (2010).
- [42] C. Bena and L. Simon, *Phys. Rev. B*, **83**, 115404 (2011).
- [43] T. Li and Z. Zhang, *J. Phys. D: Appl. Phys.*, **43**, 075303 (2010).
- [44] F. Libisch, S. Rotter, and J. Burgdörfer, “Edge scattering in graphene nanoribbons,” (2011), arXiv:1104.5260.
- [45] M. Y. Han, B. Özyilmaz, Y. Zhang, and P. Kim, *Phys. Rev. Lett.*, **98**, 206805 (2007).
- [46] G. Montambaux, F. Piéchon, J.-N. Fuchs, and M. Goerbig, *Phys. Rev. B*, **80**, 153412 (2009).
- [47] G. Montambaux, F. Piéchon, J.-N. Fuchs, and M. Goerbig, *Eur. Phys. J. B*, **72**, 509 (2009).